Effects of oxygen-related damage on dwell-fatigue crack propagation in a P/M Ni-based superalloy: from 2D to 3D assessment

R. Jiang[1], D. J. Bull[1], D. Proprentner[2], B. Shollock[2], P. A. S. Reed[1]

[1]Materials Research Group, Faculty of Engineering and the Environment, University of Southampton, Highfield, Southampton, SO17 1BJ, UK

[2] International Digital Laboratory, WMG, University of Warwick, Coventry, CV4 7AL, UK

*Corresponding author. Tel: +44 (0)23 80594438; Fax: +44 (0)23 80593016;

Email: Rong.Jiang@soton.ac.uk

Abstract Effects of oxygen-related damage (*i.e.* oxidation and dynamic embrittlement) on fatigue crack propagation behavior in an advanced disc alloy have been assessed in air and vacuum under dwell-fatigue conditions at 725 ^{o}C. The enhanced fatigue crack propagation is closely related to oxygen-related damage at/ahead of the crack tip, which is determined by the testing environment, the dwell period and the crack propagation rate itself based on two dimensional (2D) observation of the crack tip in an optical microscope and scanning electron microscope. X-ray computed tomography has also been employed to examine the differences between three dimension (3D) crack morphology in air and vacuum conditions, and the crack features have been quantified in terms of crack opening displacements, secondary cracks and uncracked bridging ligaments. The results show that the fatigue crack propagation rate is related to the amount of secondary cracks, and the crack length increment in a loading cycle is related to the breaking/cracking of the uncracked bridging ligaments within the discontinuous cracking zone ahead of the crack tip as oxygen-related damage preferentially occurs in these highly deformed regions. By combination of 3D X-ray computed tomography and traditional 2D observation, a deeper understanding is provided of the mechanisms of oxygen-enhanced fatigue crack propagation behavior.

Keywords: Ni-based superalloys; Fatigue crack propagation rate; Oxygen-related damage; X-ray computed tomography; Secondary cracks

1. Introduction

Powder metallurgy (P/M) Ni-based superalloys have been widely used for High Pressure (HP) disc rotor applications in aeroengines due to their excellent combined properties, *i.e.*

high strength at elevated temperatures, good resistance to fatigue, creep, oxidation and corrosion [1, 2]. Among all the properties of P/M Ni-base superalloys for disc applications, fatigue is one of the most important, often limiting the overall service life. However, due to the increased operating temperatures of HP discs, required to improve engine efficiency, creep and oxygen-related damage (*i.e.* oxidation and dynamic embrittlement) make increasing contributions to the fatigue failure processes of disc superalloys, especially under dwell-fatigue conditions, resulting in accelerated fatigue failure in terms of shorter fatigue life and/or faster crack propagation (FCP) rate [3-14]. Such a phenomenon is usually associated with intergranular fracture resulting from the interaction between grain boundary (GB) oxidation/embrittlement effects and mechanical fatigue processes, and is a function of the microstructures of the investigated disc superalloys and the service conditions [3-5, 15-19].

Extensive studies have been conducted to investigate the influence of oxidation on FCP under dwell-fatigue conditions. Conventionally, FCP rate has been measured by a direct current potential drop (DCPD) method, which is a measurement of the overall *averaged* crack length of the through-cracked area [20, 21]. It is usually observed that the FCP rate can be 2~3 orders of magnitude higher in the oxidising environment than that in vacuum or an inert atmosphere [4, 6, 11, 22-24], even though the DCPD method usually underestimates the crack length and the accuracy of the DCPD measurement is biased by crack front curvature and tortuosity (especially in the case where oxidation-assisted FCP is dominant, due to crack branching at the propagating intergranular crack tip or micro-cracking processes ahead of the crack tip with interlinked uncracked ligaments) [21, 25, 26]. This enhanced FCP is usually associated with the dwell period either at the maximum or minimum load employed during the test and the test temperatures in an oxidising environment [5, 6, 13]. By interrupting the fatigue tests at particular ΔK levels, the crack tips can be obtained, which can be further examined under electron microscopy to reveal the oxidation at/ahead of the crack tip. In a few recent studies, the crack tips obtained in interrupted fatigue tests or sustained load tests at elevated temperatures have been carefully examined by traditional metallographic sectioning from the center of the bulk material and/or focussed ion beam (FIB) milling on the mid-sectioned plane in combination with composition analysis of grain boundaries at/ahead of the crack tip using X-ray photoelectron spectroscopy (XPS), energy-dispersive X-ray spectroscopy (EDX), and atom probe tomography (APT) [17, 27-32]. An oxide intrusion with layered oxide structure at the crack tip and/or an oxidation damage zone ahead of the crack

tip with a size ranging from ~200nm to a few microns has been identified, providing evidence of stress/strain assisted grain boundary oxidation (SAGBO) [17, 27, 29, 32]. However, compared with the FCP rate at the investigated crack tip/ΔK level based on DCPD measurement in studies [17, 28, 31, 32], the identified oxide intrusion and/or oxidation damage zone seems to be too small to produce such rapid crack propagation, even though it may be expected that the oxide intrusion fails repeatedly during the hold period at the relatively high ΔK level.

As a counterargument to SAGBO at the crack tip, McMahon [15, 30] suggested that enhanced crack propagation should be interpreted as occurring by dynamic embrittlement, otherwise it would require unreasonably high intergranular oxygen diffusion coefficients to achieve such long-range diffusion ahead of the crack tip. The dynamic embrittlement mechanism is associated with reduction in cohesion strength of GBs ahead of the crack tip within a small scale (normally tens of nanometres) due to oxygen segregation at the GBs. It is illustrated that cracking by dynamic embrittlement is related to the uncracked ligaments at/ahead of the crack tip which hold the crack face together. The fast fatigue crack advance actually occurs in a region where intergranular cracking has already existed, rather than a damage zone comprising oxygen-weakened boundaries. As the uncracked ligaments are still electrically conductive, it is difficult to detect this cracking by DCPD methods. This dynamic embrittlement mechanism seems to be reasonable, especially at the high ΔK level which is usually associated with fast crack propagation, which limits the available time for oxidation to occur [14]. At relatively low ΔK levels, crack propagation rates are lower, providing longer times for oxygen to diffuse along grain boundaries and to form grain boundary oxides.

However, it should be noted that the aforementioned studies were all based on two-dimensional (2D) observations, which may not be fully representative of the actual crack tip due to the complexity of the crack morphology in three-dimensions (3D). In addition, depending on the stress state/ΔK at the crack tip and the selected plane/region for the metallographic sectioning/FIB milling, the observed oxidation/embrittlement at the crack tip may vary to some extent. Moreover, as the oxygen is delivered to the crack tip via the crack wake, a visualisation of 3D crack morphology is helpful to understand the transport of oxygen from the environment to the crack tip at a given FCP rate. Thus it is necessary to take the 3D crack tip morphology into consideration when evaluating the oxygen-related damage at the crack tip and linking it to the observed FCP behavior.

X-ray or synchrotron radiation computed tomography (CT) has been increasingly used in materials science investigations and has been used to characterise crack behavior in 3D [33-39]. Although X-ray CT can provide deeper insight into local crack propagation behaviors and has been shown to do so in metallic materials such as aluminium [35-37], its application to Ni-based superalloys has been hindered by Nickel's greater X-ray attenuation properties. To achieve this requires a combination of X-ray equipment with higher energies and reducing the test samples' cross-section [33]. Recent advances in X-ray imaging hardware and imaging techniques have now made this possible as outlined further in this paper. In addition to CT scanning of materials to understand their 3D behavior, there has been a push for more advanced 3D quantification techniques. A review by E. Maire and P.J. Withers [33] covers quantitative X-ray tomography techniques in more detail

In this study, the effects of oxygen-related damage on FCP behavior in an advanced disc alloy, *i.e* Low Solvus High Refractory (LSHR), has been assessed by both traditional 2D methods and 3D techniques. This work presents a first of a kind study using X-ray CT to look at the effects of oxygen-related damage in Ni-based superalloys on FCP behavior and complements 2D assessments to better understand the link between oxygen-related damage mechanisms at/ahead of the crack tip and FCP behavior.

2. Materials and experimental procedures

2.1 Materials

The LSHR alloy used in this study was provided by NASA. Composition (in wt.%) of the LSHR alloy is 12.5Cr, 20.7Co, 2.7Mo, 3.5Ti, 3.5Al, 0.03C, 0.03B, 4.3W, 0.05Zr, 1.6Ta, 1.5Nb, Ni bal. The specimens used for the FCP tests were extracted from a turbine disc which was fabricated by canning atomized LSHR alloy powder followed by hot isostatically pressing, extruding and isothermally forging. The extracted specimens were supersolvus heat treated at 1171 ^{o}C for 2 h to dissolve all γ' followed by a cooling of 72 ^{o}C/min which sets the size of the secondary γ'. Subsequently the specimens were aged at 855 ^{o}C for 4 hours and then 775 ^{o}C for 8 hours to complete the precipitation of tertiary γ'. The LSHR alloy was etched by Kalling's reagent (80ml HCl + 40ml CH_3OH + 40g $CuCl_2$) for about 10 seconds after being ground and polished to reveal grain boundaries, and was electro-etched in a solution of 10% orthophosphoric acid in H_2O at a voltage of 2 V for 25 seconds to reveal secondary γ'. The microstructures of the LSHR alloy were observed under an Olympus BH2

optical microscope and a JSM 6500F field emission gun (FEG) scanning electron microscope (SEM). The obtained microstructures of the LSHR alloy are shown in Fig. 1.

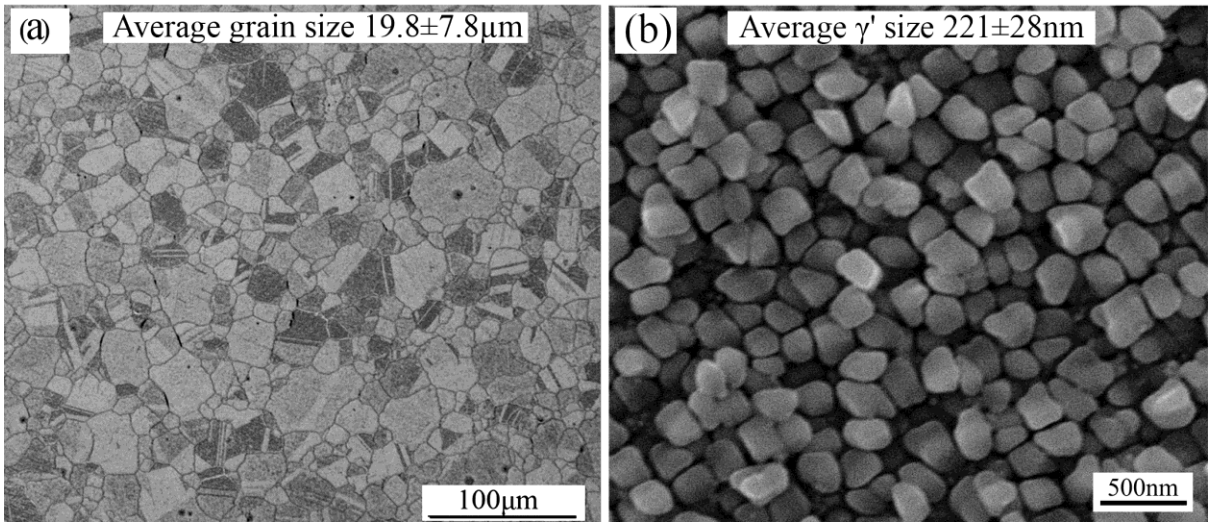

Fig. 1 Microstructures of the LSHR alloy: (a) grain morphology and (b) secondary γ' morphology.

2.2 Fatigue crack propagation tests

FCP tests were conducted on single edge notched bend (SENB) specimens with dimensions of 53.3 mm × 10 mm × 10 mm. A through thickness notch with a depth of 2.5 mm was machined by electrostatic discharge machining (EDM) in the middle of the specimen, acting as a stress concentrator to initiate the crack during the test. Both side surfaces of the specimen were polished for visualisation of oxidation interactions with the crack tip and the microstructure during the test. Tests were conducted under three-point bending on an Instron 8501 servo-hydraulic testing machine with an ESH Ltd. high temperature vacuum chamber attached under load control in both air and vacuum at 725 ^{o}C with a trapezoidal loading waveform of 1-90-1-1 at a stress ratio R=0.1. FCP tests were also conducted under waveforms of 1-300-1-1 in air and 1-20-1-1 in vacuum for comparison purposes. The test matrix is shown in Table 1. The set-up of the specimen in the test rig is schematically shown in Fig. 2 (a) and the applied loading waveform is schematically shown in Fig. 2 (b). As shown in Fig. 2 (b), the loading waveform incorporates a 1*s* loading ramp from minimum load up to maximum load, an *x* (i.e. 20, 90, 300) *s* dwell at maximum load, a 1*s* unloading ramp from maximum load down to minimum load and a 1*s* dwell at minimum load. The specimen was pre-cracked at ambient temperature using a load shedding method. The details of the pre-cracking procedure can be found in [6]. After pre-cracking, the

specimen was heated to 725 ^{o}C using four high intensity quartz lamps. The temperature of the specimen was monitored and controlled to ±1 ^{o}C using a Eurotherm 815 thermo-controller and R-type (platinum + 13% rhodium/platinum) thermocouple which was spot welded to the specimen within the hot zone. For the vacuum tests, an evacuation process was applied to evacuate the ESH Ltd. chamber to ~5×10^{-4} mbar or lower after pre-cracking, and then followed by heating. When the desired testing conditions were reached, the crack was allowed to propagate under a fixed loading amplitude. Crack length was monitored and recorded by a DCPD method using 4 probe wires. The FCP rates were derived from the curve of the variation in the electrical potential with time by the secant method. Intergranular fracture is expected to occur in air under the employed loading waveforms (based on our previous study of the two LSHR alloy variants with coarse and fine grains respectively in air under 1-20-1-1 loading waveform [6]), thus only one test under the loading waveform of 1-90-1-1 in vacuum was run to fracture for fractographic observation in this study. Other tests were stopped before final specimen fracture to examine oxidation/embrittlement at the crack tip and 3D crack morphology. The tests were paused for a short period, and the isotope of oxygen, *i.e.* $^{18}O_2$, was introduced into the chamber. After that, the tests were resumed for a further 5 loading cycles in an environment of air+$^{18}O_2$. The $^{18}O_2$ was used to act as a tracer to investigate the diffusion of oxygen at the crack tip which was then to be examined by secondary ion mass spectroscopy (SIMS). However, in this paper we are going to focus principally on the oxygen enhanced FCP behavior and the associated 3D crack morphology. The detailed study of the elucidation of the oxidation/embrittlement mechanism operating at the crack tip using $^{18}O_2$ will be presented in another paper [40].

Table 1 Fatigue test matrix of the LSHR alloy

Test conditions	Loading waveform	Environment	Maximum applied load	ΔK at the end of the fatigue test
Un-interrupted test	1-90-1-1	vacuum	2.91	Fracture
Interrupted test	1-20-1-1	vacuum	3.464	~40
	1-90-1-1	vacuum	3.086	~40
	1-90-1-1	Air	2.44	~44
	1-300-1-1	Air	2.26	~16
	1-300-1-1	Air	2.224	~28

Note: ΔK was calculated based on the post-test measurement of the crack length.

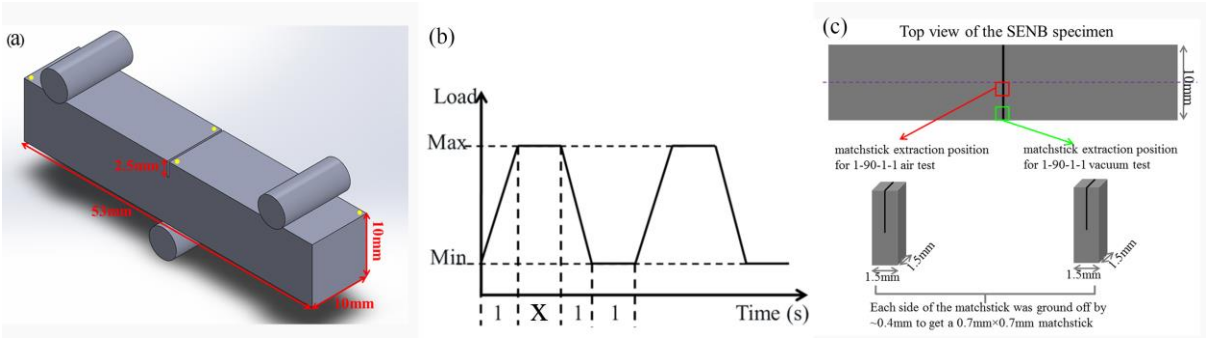

Fig. 2 (a) Schematic diagram of three-point bending test. The small yellow circles on the top surface indicate the location of electrical potential wires. (b) Schematic diagram of the loading waveform. And (c) Schematic illustration of extraction position of the "matchstick" for CT scanning from the specimens tested under 1-90-1-1 loading waveform in air and vacuum respectively.

The fracture surfaces were examined in a JEOL JSM 6500 FEG-SEM at an accelerating voltage of 15kV. Oxidation at the side surfaces in these un-fractured specimens was observed in the OM and SEM. After that, the specimens were sectioned by EDM, and then were ground and polished. The oxidation at/ahead of the crack tip in the bulk material was examined in the SEM along with EDX analysis.

2.3 Characterisation and assessment of 3D cracks by X-ray computed tomography

2.3.1 X-ray CT: material preparation and scanning parameters

X-ray CT was employed to evaluate the 3D morphology of the cracks. Due to the high X-ray attenuation of Nickel, regions of interest ("matchstick" specimens) were extracted to minimise the cross-sectional area to 0.7 × 0.7 mm^2 as schematically shown in Fig. 2 (c). Matchsticks were cut from the tested coupons under a 1-90-1-1 loading waveform which were stopped at a similar ΔK level (*i.e.* ΔK ~40 MPa√m) at the crack tip for both air and vacuum conditions. It should be noted that the high ΔK levels evaluated (~40 MPa√m) are not necessarily representative of FCP behavior at lower ΔK levels. To generate the matchstick, a section approximately 1.5 × 1.5 mm^2 was first cut off before being carefully ground down to the desired dimensions 0.7 × 0.7 mm^2. It should be noted that the matchstick was extracted from a central region in the specimen tested in air, whereas the matchstick was extracted from a region closer to side surface in the specimen tested in vacuum as schematically shown in Fig. 2 (c). However, it is believed that this slight variation of matchstick extraction site will not introduce significant differences when evaluating the

effects of environmental damage on crack tomography/geometry from CT scanning. Both matchsticks were extracted from the bulk material (e.g. the vacuum matchstick was still 0.4mm from the outer surface) and so were subjected to plane strain conditions during the tests. After the matchsticks were prepared, they were scanned using an Xradia Versa CT scanner using the following parameters: 30 second exposure, 160 kV, 10 W, 2× detector binning, 1501 projections, 0.8 µm voxel resolution. This led to a field of view of approximately 0.8 × 0.8 × 0.8 mm^3 and a scan time of approximately 15 hours per scan. To maximise X-ray flux, the source and detector were brought close together ~ 20 mm

To maximise the field of view over the length of the cracks, five regions of interest were scanned along the length of each matchstick with approximately 75 µm overlap. This led to a total scan time of approximately 75 hours per test coupon. Due to the long scan times involved, only two specimens (*i.e.* 1-90-1-1 air and 1-90-1-1 vacuum tests) were studied using X-ray CT.

2.3.2 X-ray CT: Image processing and quantification

Following acquisition of CT data, the five local scans along the length of each sample were first stitched together to create a single volume containing a larger field of view. Next, cracks were segmented out in VG-Studio using a combination of global thresholding using the ISO 50% technique [41], and seeded region growing techniques. This generated a binary volume of data containing the crack geometry.

To quantify fatigue crack propagation behavior, the following three features of the 3D crack were measured: crack opening displacements (CODs), the extent of secondary cracks, and uncracked bridging ligaments (which refers to the *uncracked* regions between two crack segments). In addition, due to the complexity of the crack tip, especially at elevated temperatures in air under dwell-fatigue conditions [21, 26], the crack tip has now been defined as “the tip of the continuous and fully opened crack” and the discontinuous cracking zone is considered to be the region ahead of the continuous crack tip with discontinuous cracks to allow more precise description (and clarity) in this paper.

1. **Crack openings** were measured by projecting the number of voxels representing the crack along a line perpendicular to the crack face (direct ray casting technique); this generated a 3D contour plot of the openings [37, 38].

2. **Secondary cracks** were quantified using a MATLAB script which identified local discontinuities on the crack opening displacement contour map. Where a secondary crack was present, the occurrence of two or more overlapping cracks when summed together gave a locally larger crack opening displacement reading. Exploiting this behavior, the extent of secondary cracks can be systematically quantified. By binning the data into 0.2 mm subsets, the extent of secondary cracking can be plotted at regions from the crack wake to the crack tip and to the discontinuous cracking zone.
3. **Crack bridging** behavior was quantified using a MATLAB script that measured the spacing between crack segments (uncracked ligaments) in the discontinuous cracking zone. The shortest distances between each crack segment were measured automatically and summed together to give the total extent of ligament interconnectivity within each subset. To observe how the extent of uncracked ligaments diminished towards the crack wake, subset binning was used at 158 μm intervals. Further details on the crack bridging method can be found in work by D.J. Bull et al [39] .

3. Results

3.1 Fatigue crack propagation behavior

Fig. 3 presents the FCP rate and the crack length evolution with the loading time in the LSHR alloy. Similar to our previous findings in this alloy, albeit in different microstructural variants, oxygen-related damage has a significant influence on FCP. As shown in Fig. 3 (a), the influence of dwell time at the peak load on FCP is not significant in vacuum. The FCP rate in vacuum under the 1-90-1-1 loading waveform is only marginally higher than that under the 1-20-1-1 loading waveform. But by changing the testing environment from vacuum to air, the FCP rate is enhanced by about two orders of magnitude as shown in the 1-90-1-1 air and vacuum tests. In air, the dwell time at the peak load exerts a more evident influence on FCP than in vacuum as indicated by the 1-90-1-1 test and the 1-300-1-1 test.

Fig. 3 (b) shows the crack length evolution with the *relative* time under load cycling. The corresponding ΔK at the beginning and end of the selected load cycling time is indicated on the graph. As shown in Fig. 3 (b), two different patterns of crack length evolution with time under load cycling in air and vacuum can be identified. In the air tests either under the 1-90-1-1 or the 1-300-1-1 loading waveform, the crack length increment mainly occurs at the end of the dwell period (*i.e.* the unloading and re-loading stage) at the low ΔK level, and no

evident dwell stage can be discerned due to the small crack length increment in a loading cycle. As crack length (ΔK) increases, the crack length increment during the unloading and reloading stage after a dwell period becomes more evident, this makes the dwell stage more apparent. In an individual loading cycle in the mid-range of the ΔK level, no apparent crack length increase during the dwell period is spotted. As crack length (ΔK) further increases, a continuous crack length increase can be seen during the dwell period at the peak load as shown in the 1-90-1-1 air test. Conversely, the vacuum test under the 1-90-1-1 loading waveform shows a completely different pattern during most stages of fatigue crack propagation. A quite significant crack length reduction (which is associated with crack closure during the unloading stage) is observed during the unloading and reloading stage after a dwell period, and then the crack is kept open during the dwell period at the peak load, showing the pattern of crack response to the loading in an individual cycle. However, it is interesting to notice that intermittently there is a significant increase in crack length after a particular dwell period in vacuum as shown in the inset graph at the top-left corner in Fig. 3 (b). After this dramatic crack length increase, the crack shows some evidence of closure behavior and then a similar crack length evolution pattern can be seen again. The different responses of the cracks to the loading in an individual loading cycle in air and vacuum indicate the different cracking mechanisms operating at the crack tip.

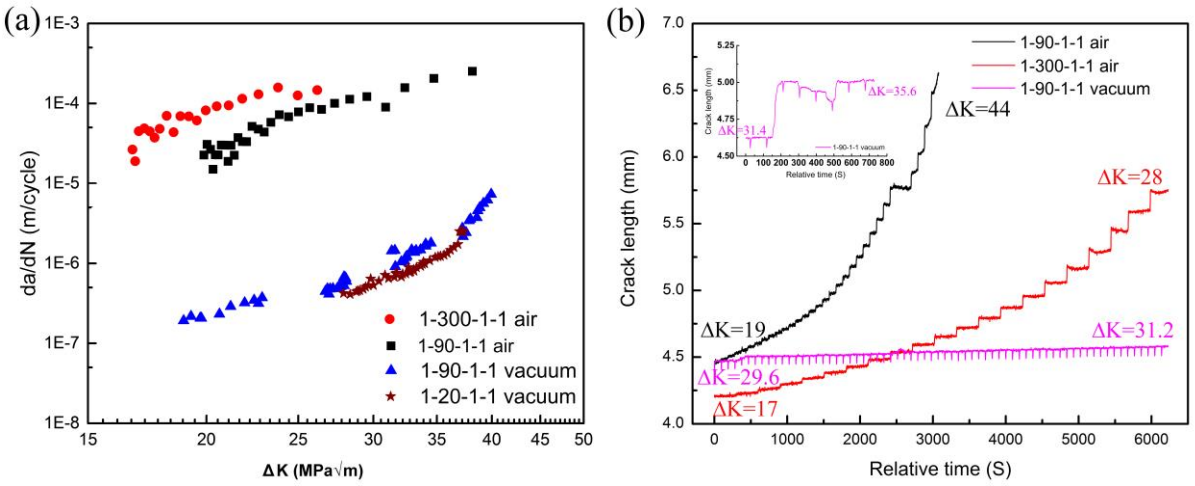

Fig. 3 (a) Fatigue crack propagation rate and (b) the crack length evolution with the loading time in the LSHR alloy.

The fractography of the 1-90-1-1 vacuum test is shown in Figs. 4 (a) and (b). The fractography of the 1-20-1-1 vacuum test from our previous study [6] on the LSHR alloy variant (which has a coarser grain size) is also presented in Figs. 4 (c) and (d) for comparison.

As shown in Fig. 4, the fracture surfaces in both cases show mixed inter-transgranular fracture. The presence of partially intergranular failure in the vacuum tests is probably due to the relatively poor vacuum (i.e. 5×10^{-4} mbar) and high test temperature (i.e. 725 °C) in these tests which allow some environmental degradation to still take place. It appears that the fracture surface of the 1-90-1-1 vacuum test in this study appears to be more intergranular and rougher than that in 1-20-1-1 vacuum test. This might be associated with the longer dwell time at the peak load and the relatively smaller grain size of the LSHR alloy used in this study.

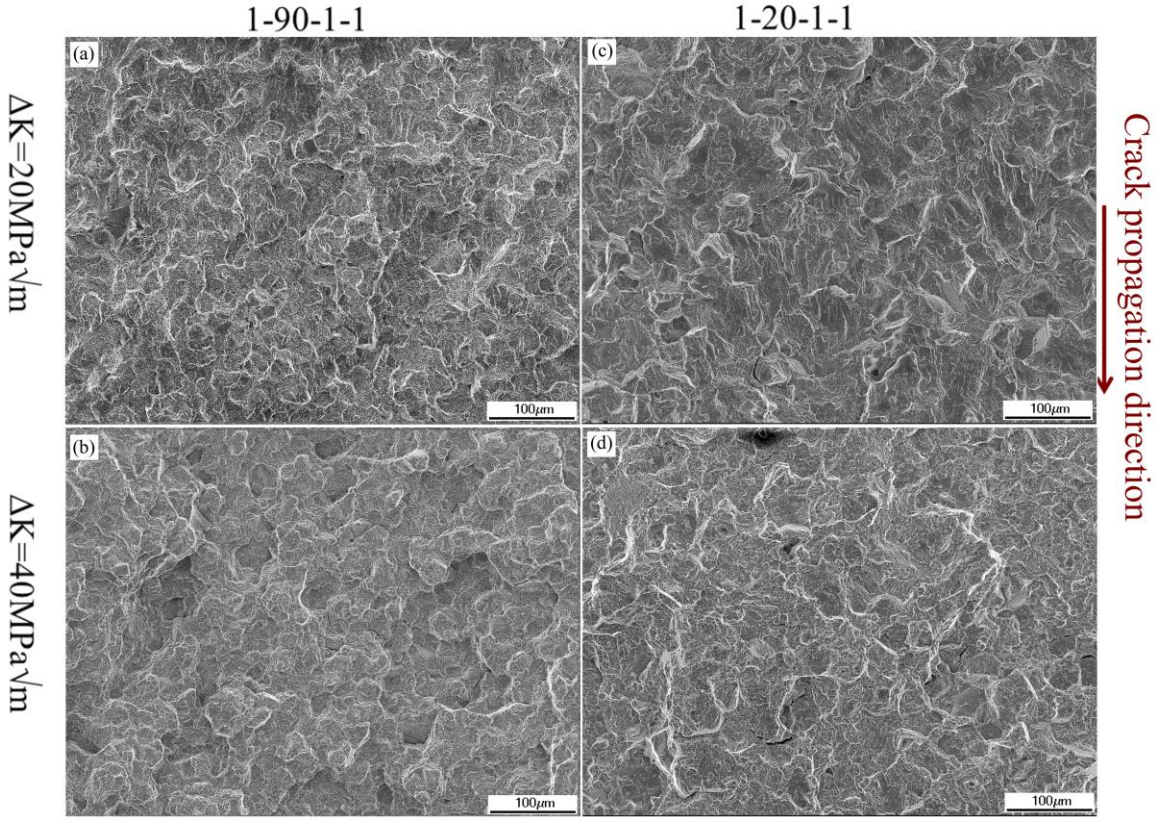

Fig. 4 Fractography of vacuum tests: (a) 1-90-1-1, ΔK=20 MPa√m; (b) 1-90-1-1, ΔK=40 MPa√m; (c) 1-20-1-1, ΔK=20 MPa√m [6]; and (d) 1-20-1-1, ΔK=40 MPa√m [6].

Oxidation processes at the crack tip on the side surface and in the center of the bulk material in both vacuum and air tests has been examined by OM and SEM. As shown in Fig. 5 (a), even in vacuum under a loading waveform of 1-90-1-1, oxidation can still be discerned on the side surface at the crack tip and in the crack wake. Grain boundaries are visible on the side surface due to a thermal etching effect. The EDX analysis indicates that the oxides formed at the crack tip and crack wake at the side surface are Cr-rich oxides. Figs. 5 (b) and (c) present the morphology at the crack tip on the side surface in the 1-90-1-1 air test, from

which we can see a branched crack tip. Unlike the vacuum test, oxidation at the crack tip on the side surface in the air testing condition is much more significant. Bulged grain boundary oxides are seen at the crack tip (as indicated in Fig. 5 (c)). These bulged grain boundary oxides are Co and Ni-rich oxides as shown in our previous studies where FIB extraction of TEM lamellar containing bulged grain boundary oxides characterised the oxides in the TEM using EDX [12, 18]. Due to the oxidation, an inverted "V" shape oxidation damage zone is discerned at the crack tip on the side surface which appears to be associated with the expected plastic zone at the crack tip. This characteristic inverted "V" shape showing possible plastic lobes at the crack tip form a distinct oxidation damage zone on the side surface. Fig. 5 (d) shows the crack tip in the bulk material seen in the center, obtained after sectioning the specimen tested in air. The crack tip in the bulk material appears to be a much simpler geometry than seen on the side surface, but an intergranular crack path is still found in the bulk material. However, it should be borne in mind that the difference in crack tip geometry observed between the side surface and center may also depend on which plane was sectioned, and does not reflect the true 3D crack geometry. EDX examination of the crack tip in the center shows little enrichment of O at the grain boundary at the crack tip.

Figs. 5 (e) - (h) present the crack tip morphology in the 1-300-1-1 air tests. Similarly to the 1-90-1-1 air test, bulged grain boundary oxides can be found on the side surface at the crack tip either at ΔK of ~16 MPa$\sqrt{m}$ or ~28 MPa$\sqrt{m}$ as shown in Figs. 5 (e) and (g) respectively, and the intergranular crack tip morphology seen in the bulk material is also simpler than that observed on the side surface as shown in Figs. 5 (f) and (h). An inverted "V" shape oxidation damage zone is also found at the crack tip at a ΔK of ~28 MPa$\sqrt{m}$ (Fig. 5 (g)), even though it is not as evident as seen in the 1-90-1-1 air test (Fig. 5 (b)) due to the lower ΔK level at the crack tip (and hence the smaller plastic zone size). Examination of oxidation at the crack tip in the bulk material using EDX shows that an apparent enrichment of O is found at the crack tip at a ΔK of ~16 MPa$\sqrt{m}$, but no O enrichment is found at the crack tip at a ΔK of ~28 MPa$\sqrt{m}$. This difference indicates that FCP rate (which affects the available oxygen diffusion time at/ahead of the crack tip before the crack advances through the embrittled region) also has an influence on the observed oxidation damage process at/ahead of the crack tip. However it should be noted that the absence of O detection at the crack tip at relatively high ΔK levels may be related to insufficient resolution of EDX and/or the relatively fast crack propagation rate which results in less apparent oxide forming. Detailed examination and

analysis of the oxygen distribution at/ahead of the crack tip using ^{18}O distribution will be presented in detail in a further paper [40].

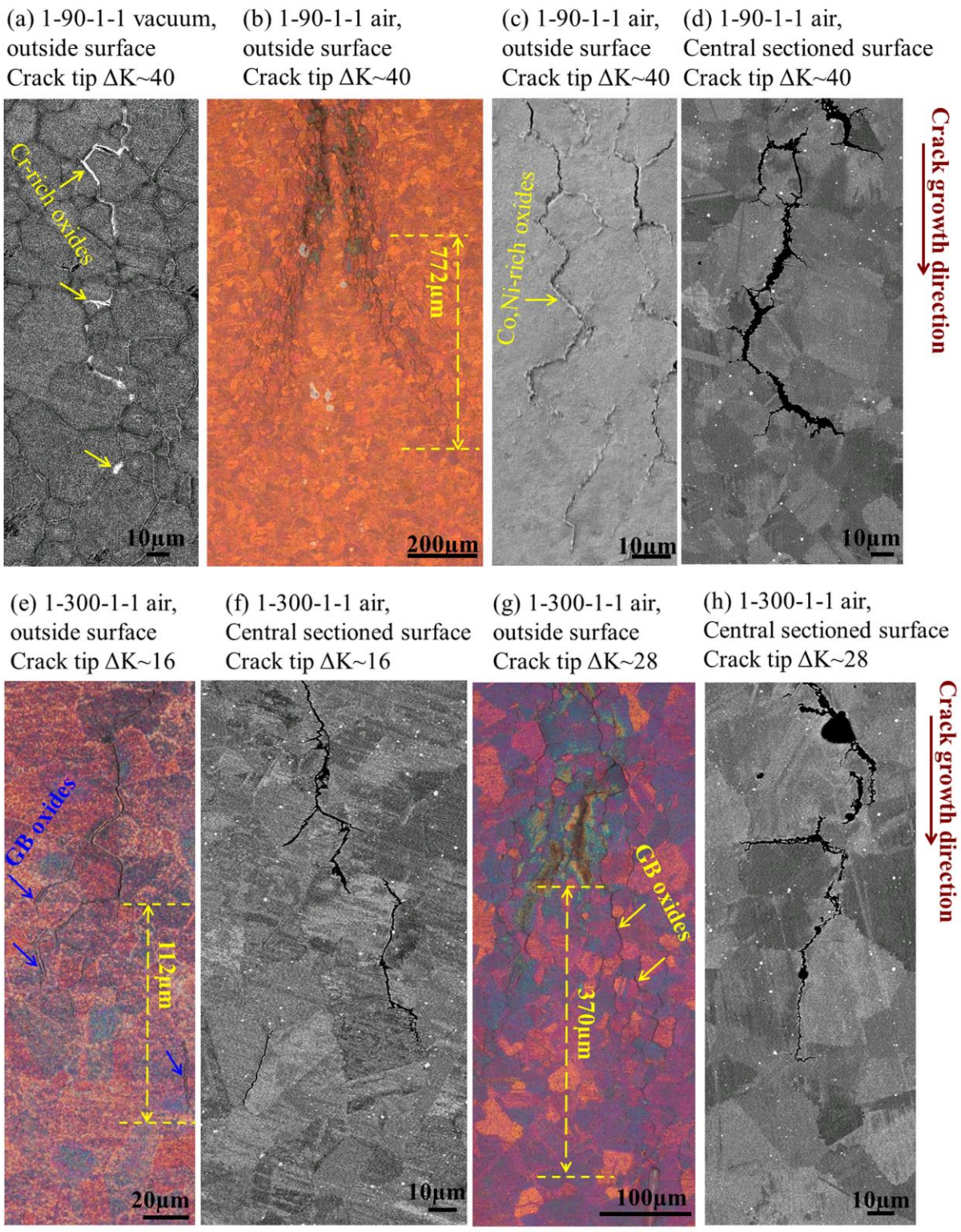

Fig. 5 Crack tip at side surface and central sectioned surface: (a) 1-90-1-1, vacuum, outside surface, ΔK~40 MPa√m; (b) and (c) 1-90-1-1, air, outside surface, ΔK~44 MPa√m; (d) 1-90-

1-1, air, central sectioned surface, ΔK~44 MPa√m; (e) 1-300-1-1, air, outside surface, ΔK~16 MPa√m; (f) 1-300-1-1, air, central sectioned surface, ΔK~16 MPa√m; (g) 1-300-1-1, air, outside surface, ΔK~28 MPa√m; (h) 1-300-1-1, air, central sectioned surface, ΔK~28 MPa√m.

The measured oxidation damage zone size at the crack tips on the side surfaces in the air tests is shown in Table 2 and is indicated in Fig. 5. The monotonic ($r_{p,monotonic}$) and cyclic ($r_{p,cyclic}$) plastic zone sizes (PZS) at the crack tip were calculated using Irwin's approximation based on a plane stress assumption with Equations (1) and (2) [42], and are also presented in Table 2 to make a comparison with the measured oxidation damage zone at the side surface .

$$r_{p,monotonic} = \frac{1}{\pi}\left(\frac{K_{max}}{\sigma_y}\right)^2 \quad (1)$$

$$r_{p,cyclic} = \frac{1}{\pi}\left(\frac{\Delta K}{2\sigma_y}\right)^2 \quad (1)$$

where K_{max} is the maximum stress intensity factor at the crack tip and σ_y is the yield stress of LSHR alloy. The measured oxidation damage zone size on the side surfaces is close to the calculated monotonic plastic zone size, which suggests there could be effects of plastic deformation on oxide formation. However, it should be noted that the precise location of the crack tip at the side surface cannot be identified accurately due to its branched nature. Hence, the measured oxidation damage zone size may be somewhat overestimated.

Table 2 Measured oxidation damage zone size and calculated monotonic and cyclic plastic zone size at the crack tip on the side surfaces.

	Measured oxidation damage zone size(μm)	Calculated monotonic PZS (μm)	Calculated cyclic PZS (μm)
1-90-1-1 air ΔK=44 MPa√m	772	769	156
1-300-1-1 air ΔK =16 MPa√m	112	102	21
1-300-1-1 air ΔK =28 MPa√m	370	312	63

3.2 3 D assessment of fatigue cracks from CT scans: qualitative and quantitative results

Two LSHR specimens were studied in detail using 3D X-ray CT. These consisted of one specimen loaded in air and the other in vacuum under a 1-90-1-1 waveform. Data from the

CT scans has allowed the 3D crack features to be qualitatively and quantitatively studied to identify key differences and understand how oxygen-related damage affects crack behavior.

Figs. 6 (a) and (b) show an X-ray CT cross-section of the main crack in air and vacuum conditions respectively. Two key features can be identified from the cross-sections: secondary cracking in the crack wake and bridging ligament formation (uncracked ligaments) caused by discontinuous cracks within the discontinuous cracking zone ahead of the crack tip. These two features were present in both specimens and are quantified further later to understand the extent of these features.

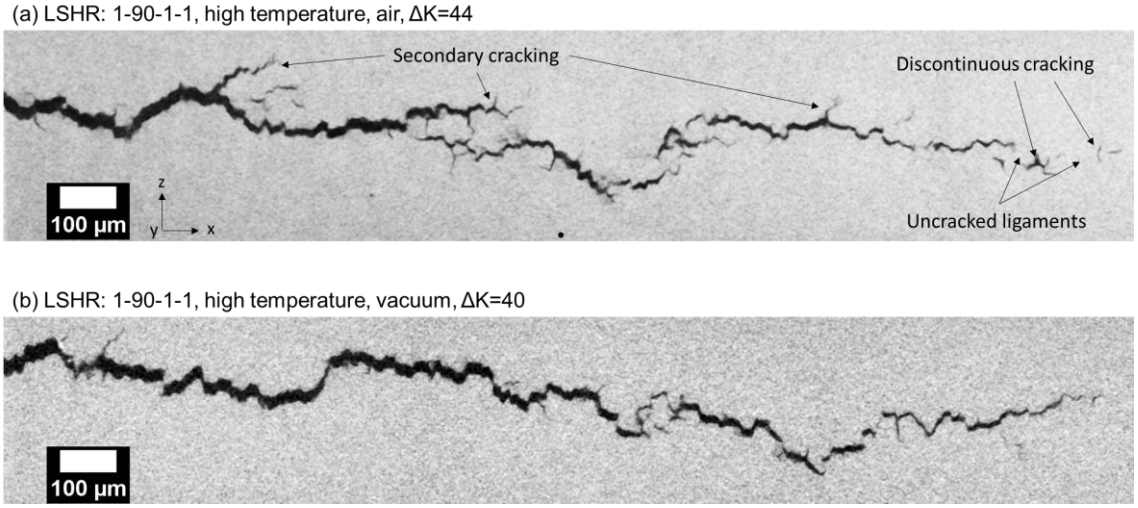

Fig. 6 CT cross-sections of LSHR 1-90-1-1 test in (a) air and (b) vacuum at 725 ^{o}C.

3D renderings of the cracks are shown in Fig. 7 for (a) air and (b) vacuum conditions. From this image, the overall geometry of the cracks can be observed including the overall roughness present in both cracks. It appears that the crack front in air is more symmetrical than that in the vacuum condition. It should be noted that this difference is probably related to the sampling as schematically shown in Fig. 2 (c). Although the matchstick extraction position has certain influence on the overall crack geometry, it is believed that this slight variation of matchstick extraction site should not bring significant bias when evaluating the effects of environmental damage on fatigue crack propagation mechanisms. The discontinuity ahead of the crack tip and the interlinked uncracked ligaments in the discontinuous cracking zone ahead of the crack tip can be seen in both cases. Two distinct zones are observed consisting of (a) a continuous cracking zone at the crack wake, and (b) a discontinuous cracking zone ahead of the crack tip where uncracked ligaments forming between cracks are observed. In the continuous cracking zone, a large extent of secondary cracking (cracks

forming off the main crack body) was observed in the specimen tested in air (Fig. 6 (a)). In the discontinuous cracking zone ahead of the crack tip, islands of crack segments appear completely unconnected to the main body of the crack (as can be observed in an individual CT slice shown in Fig. 6) but these regions can be discerned to be partially connected to the main crack in 3D in specimens tested in both air and vacuum.

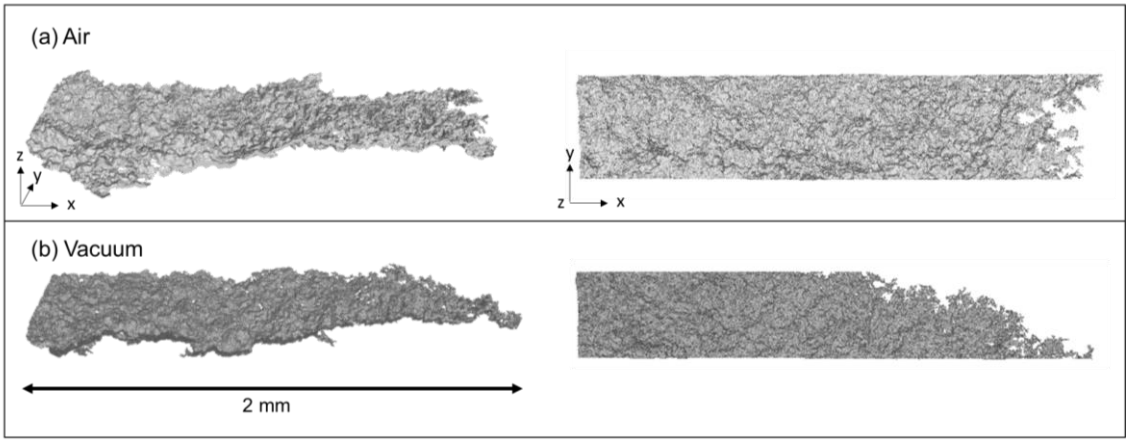

Fig. 7 CT 3D renderings of crack profile for 1-90-1-1 (a) air and (b) vacuum environment. Contained in the rendering is a 45^{o} slanted view of the crack profile (left) and a topological view of the crack profile (right).

Fig. 8 shows the CODs measured perpendicular to the crack plane. Figs. 8 (a) and (b) show a full field COD map across the specimens tested in air and vacuum respectively. Line plots across the dotted lines in Figs. 8 (a) and (b) are shown in Fig. 8 (c). One key difference is more extensive "fringed peaks" representing locally higher COD measurements. These are believed to be caused by secondary cracks which when summed together with the main crack give locally larger readings. Qualitatively, this phenomenon appears to be more extensive in the air specimen than vacuum and has been exploited later to quantify the extent of secondary cracks between these two specimens. It should be mentioned that the line plots shown in Fig. 8 (c) have been smoothed to remove the high frequency measurements and to give the general profile of the opening. In both air and vacuum cases, the general shape and magnitude of the COD are similar.

Fig. 9 presents the quantified secondary crack measurements for the specimens tested in air and vacuum. These were measured as a percentage of secondary cracks occupying an area of the projected crack in 0.2 mm subsets from the crack wake to the crack tip. It is clear that towards the crack wake, 0.5 mm behind the crack tip (i.e. the continuous cracking zone in the

crack wake), there is an extensive increase in secondary crack formation in the air test. In this continuous cracking zone, it appears that the amount of secondary cracks is about two to five times more in the specimen tested in air than that in vacuum. Within the discontinuous cracking zone ahead of the crack tip, similar extents of secondary cracking are observed.

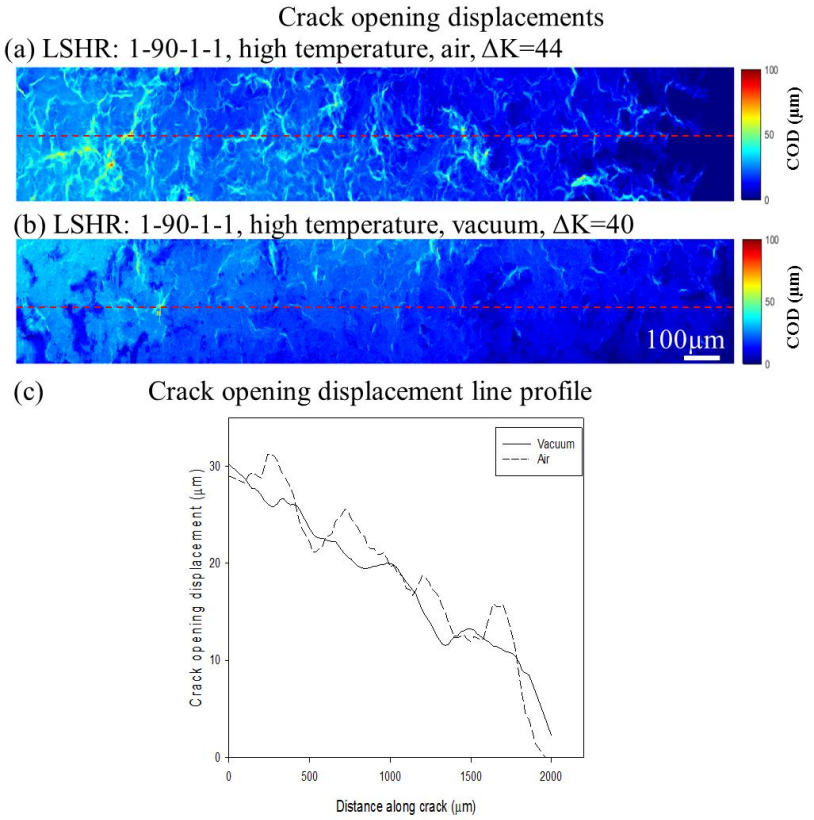

Fig. 8 Crack opening displacement plots across the crack face (crack tip on right) for LSHR alloy in (a) air and (b) vacuum under 1-90-1-1 loading waveform at 725 ^{o}C. (c) COD line profile plots as measured across the red dotted lines in (a) & (b). Line profile has been smoothed to make clearer the overall COD profile.

Fig. 10 quantifies the discontinuous crack formation ahead of the crack tip (*i.e.* uncracked bridging ligaments). The total interconnectivity area between each discontinuous crack was calculated using 158 µm subsets along the direction from the crack wake towards the crack tip. The general trend of the plots shows the diminishing extent of ligaments towards the crack wake as the crack becomes more developed and transitions into a continuous cracking zone. This occurs over a 500-micron region. Comparing the uncracked ligaments between the specimens tested in vacuum and air, it appears that the specimen tested in vacuum has ~75% more ligaments within the subset farthest away from the crack wake. However the results here are quite sensitive to the binning size and local variations within the material, so in this

respect may not be a fair comparison to make. Summing together the total ligaments across the whole 500 μm range results in similar extents of ligaments observed in both specimens (~35% difference).

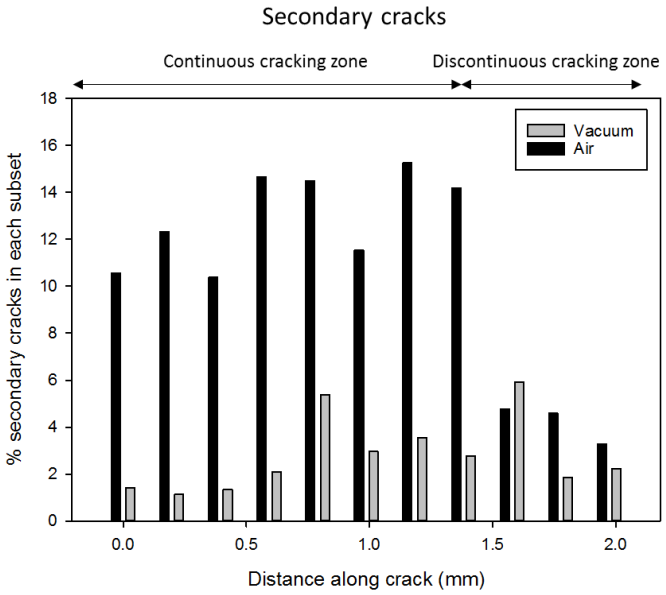

Fig. 9 Bar plot comparing the extent of secondary cracking from crack wake (left) to crack tip and to the discontinuous cracking zone (right) between the 1-90-1-1 air and vacuum tests. Two cracking zones are indicated consisting of a continuous cracking zone 0-1.5 mm and discontinuous cracking zone 1.5-2.0 mm. Subset size is 0.2 mm.

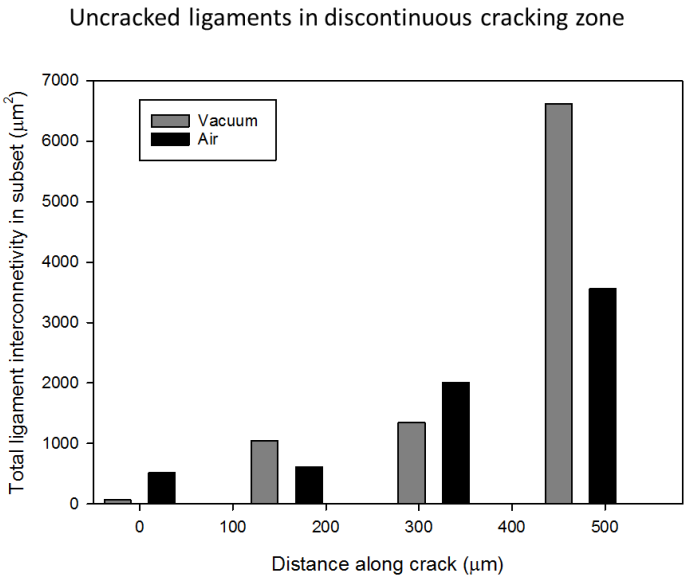

Fig. 10: Uncracked ligament quantification in the discontinous cracking zone along the direction from crack wake (left) to crack tip (right). Subset size 158 microns.

4. Discussion

Oxygen-enhanced FCP in the LSHR alloy, which is related to the testing environment and the dwell time at the peak load, is clearly illustrated in this study. This enhanced FCP is related to the increased oxidation behavior at the crack tip, which is verified by the OM/SEM examination of oxides formed at the crack tip on the side surfaces and at the crack tip in the bulk material at the relatively low ΔK levels. The measured size of the oxidation damage zone formed at the crack tip at the side surface is close to the calculated plastic zone size, indicating the effects of plastic deformation on oxidation processes and the stress/strain assisted grain boundary oxidation is the dominant mechanism controlling the enhanced FCP at the side surface under the dwell-fatigue conditions. At higher ΔK levels, although an intergranular path can be seen from the central sectioned plane in this study and an intergranular fracture surface has been observed in our previous studies on the same alloy [6], no apparent O enrichment at the crack tip in the bulk material was found. This difference between observed oxidation at the crack tip on side surface and in the bulk material indicates that the availability of oxygen at the crack tip (i.e. transport to the crack tip) plays an important role in oxidation process at the crack tip. On the side surface, due to its continuous exposure in air, the oxygen concentration (oxygen partial pressure) is high enough to facilitate the occurrence of GB oxidation under the stress/strain produced at the crack tip. However, in the bulk material, particularly within the discontinuous cracking zone ahead of the crack tip, the transport of oxygen to this region is hindered to some extent by the uncracked ligaments. As a result, no such evident oxidation zone occurs in the bulk material, especially at high ΔK level. The absence of detected O enrichment at the crack tip at high ΔK level in the bulk materials may be caused by the relatively high FCP rate which provides insufficient time for oxygen diffusion and formation of observable/resolvable oxides within the EDX detection limit (as the activated volume of EDX analysis is at μm^3 scale). Or it may be caused by the repeated cracking of the formed oxides at the crack tip at the relatively high ΔK level as proposed in [13]. Alternatively, a dynamic embrittlement mechanism may dominate the weakening process along the grain boundaries at the crack tip at relatively high ΔK levels and leads to enhanced FCP without oxides being directly formed at the crack tip. Further examination of O distribution at the crack tip at different ΔK levels is underway using SIMS and ^{18}O as a tracer element and is expected to provide a clearer mechanism map for the oxygen-enhanced FCP behavior in this alloy.

X-ray CT has been used to evaluate the 3D crack features in the Ni-based superalloy in terms of the COD, secondary cracks and uncracked bridging ligaments in this study for the first time. Whilst CT provides a lot of detail, the main limitation is the long scan time on a lab based system (75 hours per sample) and limited field of view (0.8 x 0.8 mm^2 cross-section). Such limitations make it difficult to perform high throughput studies. However the continued use of synchrotron CT facilities in the future may allow further detailed systematic data to be produced in a larger number of representative volumes under varying temperatures and dwell times. It seems that oxygen-enhanced FCP is closely related to the development of secondary cracks as indicated by the quantitative analysis of the CT data. Generally, a more oxidising environment is linked to more significant secondary cracks (Fig. 9) and faster FCP rate (Fig. 3). This is consistent with our previous study based on statistics of the observed secondary cracks on the fracture surface examined by SEM [6] and is also consistent with NASA's study on the LSHR alloy [8]. However, unlike our previous findings [6], that the amount of secondary cracks (observed from fractography) increases with ΔK, the amount of secondary cracks at the crack tip and within discontinuous cracking zone is found to be much less than that in the crack wake observed by X-ray CT. This contrast to our previous findings may arise from the immature development of the secondary cracks at the crack tip and within the discontinuous cracking zone due to the constrained crack tip in the CT scanned matchstick (vs. an unconstrained fracture surface). The lower spatial resolution achieved by X-ray CT may also underestimate the extent of secondary cracking.

Fatigue cracking processes (either the main crack advance or secondary cracking) in air under dwell-fatigue conditions are closely related to oxygen-related damage along grain boundaries at/ahead of the crack tip caused by SAGBO and/or dynamic embrittlement [4, 6, 10, 11, 15]. However, the extent of such oxygen-related damage at/ahead of the crack tip is dependent on the local oxygen partial pressure and stress/strain state whether SAGBO or dynamic embrittlement is the dominant activated mechanism. As shown in Karabela's study [43], the oxygen penetration depth into a RR1000 disc alloy depends on oxygen concentration/oxygen partial pressure and the stress state. Higher oxygen partial pressure and stress are associated with a deeper penetration distance. The fewer observed secondary cracks at the crack tip and within the discontinuous cracking zone in the air test compared with those in the crake wake indicates that oxygen transport to the crack tip and into the discontinuous cracking zone is critical for the occurrence of oxygen-related damage. It should also be noted that the total number of secondary cracks over the 500 μm range close to the crack tip is quite

close to that observed in vacuum/low oxidation conditions. This can be further supported by the extensive GB oxidation observed at the outside surface in the air test but limited GB oxidation observed in the mid-section plane as shown in Fig. 5. Based on the metallographic 2D observations and X-ray CT 3D observations of crack morphology, a schematic diagram (Fig. 11) has been drawn to illustrate the main crack advance process and secondary crack development in the air test. As schematically shown in Fig. 11 (a), for a crack with a length of *a*, within the discontinuous cracking zone ahead of the crack tip, there is insufficient oxygen arriving in this region due to the existence of the uncracked ligaments acting as barriers to the oxygen flow path, even though the discontinuous cracks are partially connected to the main crack plane in 3D as shown in Fig. 7. As a result, the discontinuous cracking zone ahead of the crack tip is under a quasi-vacuum/low oxygen partial pressure condition. Consequently, the secondary cracking within the discontinuous cracking zone ahead of the crack tip is similar to that which occurs in vacuum and mainly occurs only in the plastic zone around the crack tip. As the crack advances via breaking the uncracked ligaments (due to eventual oxygen-related damage in the uncracked ligaments) and connecting of the discontinuous crack segments, as shown in Fig. 11 (b), oxygen can relatively easily access the fully opened crack wake where the crack has just advanced and is still encompassed by the plastic zone (due to the complex surrounding 3D nature of the crack tip). With the assistance of the relatively high stress/strain of the plastic zone and the increased oxygen partial pressure, oxygen-related damage along grain boundaries occurs by SAGBO or dynamic embrittlement. As a consequence, secondary cracking starts to develop in this freshly formed crack wake as schematically shown in Fig. 11 (c). Hence, more secondary cracks are observed in the air test. As the crack tip continues to advance, the stress at this position in the crack wake diminishes and the ongoing oxygen-related damage becomes less significant until the stress becomes insufficient to continue to assist oxygen-related damage along grain boundaries and the secondary cracking process then stops at that part of the crack wake (which is now too far from the active crack tip stress state).

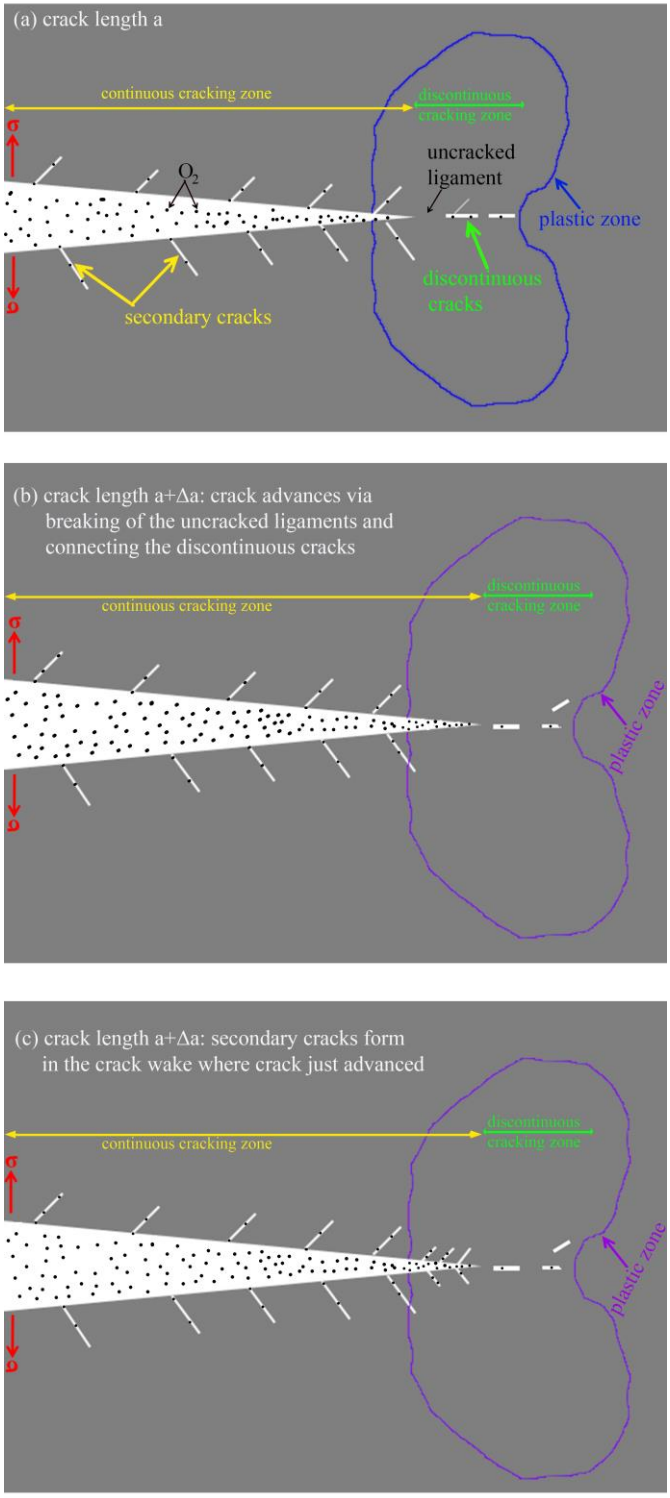

Fig. 11 Schematic diagram of crack advancement and secondary cracking formation. The plastic zone profile is sketched at the crack tip based on a simulation presented in our previous study [44]. (a) Crack tip at a crack length of *a*; (b) crack advances via breaking of the uncracked ligaments and connecting to the discontinuous cracks; and (c) secondary cracking formation in the crack wake where the crack has just advanced.

By combining the X-ray CT investigation of 3D crack morphology, DCPD crack length measurement and traditional 2D observation using optical and/or electron microscopes, a better understanding of the processes of crack propagation has been achieved. During dwell-fatigue loading at elevated temperatures, oxygen-related damage preferentially occurs in these uncracked ligaments within the discontinuous cracking zone ahead of the crack tip due to the higher degree of deformation in these regions. In other words, the uncracked ligaments in the discontinuous cracking zone ahead of the crack tip are more brittle in air than in vacuum. The crack propagation is via breaking the uncracked ligaments and connecting to the discontinuous cracks in the discontinuous cracking zone ahead of the crack tip. The observed jump in crack length evolution in air (Fig. 3b) measured by DCPD is probably related to oxygen-related damage along grain boundaries in the uncracked ligaments ahead of the crack tip during the dwell period and breaking of these embrittled ligaments during the unloading and reloading. As the crack advances, oxygen can approach this freshly formed crack wake where crack tip has just advanced and is still encompassed by the plastic zone to facilitate the development of secondary cracking. The amount of secondary cracks developed is also related to the oxygen-related damage at the crack tip which is determined by the local microstructure, oxygen partial pressure and plastic deformation at the crack tip. Generally, in the high ΔK region (which is usually associated with fast FCP), more secondary cracks are observed due to the large plastic zone at the crack tip.

5. Conclusions

In this study, FCP behavior in an advanced disc alloy, i.e. LSHR alloy, has been assessed in air and vacuum under three loading waveform conditions to reveal the effects of oxygen-related damage on FCP. X-ray CT has been employed to examine the 3D crack features, providing a first of its kind study using CT to investigate 3D crack growth behavior in Ni-based superalloys. Combining these 3D X-ray CT measurements and traditional 2D observation provides a deeper understanding of the mechanisms of oxygen-enhanced FCP. Based on this study, the following conclusions can be drawn:

Oxygen-enhanced FCP is closely related to the test environment and the dwell period at the peak load. The dwell time in vacuum only exerts a marginal effect on FCP. Oxidation preferentially occurs at the side surface and at/ahead of the crack tip at relatively low ΔK level in the bulk material. At relatively high ΔK levels, oxides are rarely detected at/ahead of the crack tip in the bulk material by EDX, and the weakening process along grain boundaries

at/ahead of the crack tip may switch from SAGBO to dynamic embrittlement due to the fast FCP reducing the time for oxidation onset in the crack tip material. Further examination of O distribution at/ahead of the crack tip at different ΔK levels is underway using SIMS and ^{18}O [40].

X-ray CT is able to extract complex 3D crack morphologies in Ni-based superalloys which informs our understanding of crack advance processes. A higher FCP rate was associated with a greater amount of secondary cracks in the crack wake in the air test, which is associated with the degree of oxygen-related damage. The crack length increase in a loading cycle measured by the DCPD method appears related to the breaking of the uncracked ligaments and connection of the main crack to the discontinuous cracks in the discontinuous cracking zone ahead of the crack tip. At elevated temperatures under dwell-fatigue loading conditions, oxygen-related damage preferentially occurs in these highly deformed bridging ligaments.

Data access statement

The raw data presented in this paper can be found via the DOI:10.5258/SOTON/D0012 (http://doi.org/10.5258/SOTON/D0012).

Acknowledgement

Thanks are due to the EPSRC (Grant EP/K027271/1) of the UK for funding support, and to NASA of US for the supply of the LSHR alloy. The authors also would like to thank Prof. Liguo Zhao at the Loughborough University, Dr. Mark Hardy at Rolls-Royce, Dr. Gordon McColvin at GE Power, Dr. Matthew Lunt at Defence Science and Technology Laboratory, Prof. Scott Lockyer and Dr. Katherine Soady at Uniper Technologies Ltd for useful discussions.

Reference

[1] R. C. Reed, The Superalloys: Fundamentals and Applications, Cambridge University Press, 2006.
[2] T. M. Pollock, S. Tin, Journal of Propulsion and Power, 22 (2006) 361-374.
[3] E. Andrieu, R. Molins, H. Ghonem, A. Pineau, Materials Science and Engineering: A, 154 (1992) 21-28.
[4] R. Molins, G. Hochstetter, J. C. Chassaigne, E. Andrieu, Acta Materialia, 45 (1997) 663-674.
[5] D. G. Leo Prakash, M. J. Walsh, D. Maclachlan, A. M. Korsunsky, International Journal of Fatigue, 31 (2009) 1966-1977.
[6] R. Jiang, S. Everitt, M. Lewandowski, N. Gao, P. A. S. Reed, International Journal of Fatigue, 62 (2014) 217-227.
[7] H. T. Pang, P. A. S. Reed, Materials Science and Engineering: A, 448 (2007) 67-79.

[8] J. Telesman, T. P. Gabb, A. Garg, P. Bonacuse, J.Gayda, Effect of Microstructure on Time Dependent Fatigue Crack Growth Behavior In a P/M Turbine Disk Alloy, In: R. C. Reed, K. A. Green, P. Caron, T. P. Gabb, M. G. Fahrmann, E. S. Huron, S. A. Woodard, Superalloys 2008. Warrendale (PA): The Minerals, Metals & Materials Society, (2008) 807-816.
[9] T. P. Gabb, J. Gayda, J. Telesman, L. J. Ghosn, A. Garg, International Journal of Fatigue, 48 (2013) 55-67.
[10] R. Jiang, S. Everitt, N. Gao, K. Soady, J. W. Brooks, P. A. S. Reed, International Journal of Fatigue, 75 (2015) 89-99.
[11] R. Jiang, P.A.S. Reed, Materials Science and Technology, 32 (2016) 401-406.
[12] R. Jiang, N. Gao, M. Ward, Z. Aslam, J. C. Walker, P. A. S. Reed, Effects of oxidation on fatigue crack initiation and propagation in an adcanced disk alloy, In: Mark Hardy, Eric Huron, Uwe Glatzel, Brian Griffin, Beth Lewis, Cathie Rae, V. Seetharaman, S. Tin, Superalloys 2016, Seven Springs (PA): The Minerals, Metals & Materials Society, (2016) 907-916.
[13] H. Y. Li, J. F. Sun, M. C. Hardy, H. E. Evans, S. J. Williams, T. J. A. Doel, P. Bowen, Acta Materialia, 90 (2015) 355-369.
[14] H. Ghonem, D. Zheng, Materials Science and Engineering: A, 150 (1992) 151-160.
[15] J. A. Pfaendtner, C. J. McMahon Jr, Acta Materialia, 49 (2001) 3369-3377.
[16] U. Krupp, W. M. Kane, C. Laird, C. J. McMahon, Materials Science and Engineering: A, 387–389 (2004) 409-413.
[17] H. S. Kitaguchi, H. Y. Li, H. E. Evans, R. G. Ding, I. P. Jones, G. Baxter, P. Bowen, Acta Materialia, 61 (2013) 1968-1981.
[18] R. Jiang, N. Gao, P. A. S. Reed, J Mater Sci, 50 (2015) 4379-4386.
[19] T. P. Gabb, J. Gayda, J. Telesman, Thermal and Mechanical Property Characterization of the Advanced Disk Alloy LSHR, NASA report NASA/TM-2005-213645, (2005).
[20] Standard Test Method for Measurement of Fatigue Crack Growth Rates, ASTM E647.
[21] E. Storgärds, K. Simonsson, Exp Mech, 55 (2015) 559-568.
[22] S. Everitt, R. Jiang, N. Gao, M.J. Starink, J. W. Brooks, P. A. S. Reed, Materials Science and Technology, 29 (2013) 781-787.
[23] S. Everitt, M. J. Starink, H. T. Pang, I. M. Wilcock, M. B. Henderson, P. A. S. Reed, Materials Science and Technology, 23 (2007) 1419-1423.
[24] J. Gayda, R. V. Miner, International Journal of Fatigue, 5 (1983) 135-143.
[25] S. Y. Yu, H. Y. Li, M. C. Hardy, S. A. McDonald, P. Bowen, Mechanisms of dwell fatigue crack growth in an advanced nickel disc alloy RR1000, Eurosuperalloys 2014–2nd European Symposium on Superalloys and their Applications, http://dx.doi.org/10.1051/matecconf/20141403002.
[26] E. Fessler, E. Andrieu, V. Bonnand, V. Chiaruttini, S. Pierret, International Journal of Fatigue, 96 (2017) 17-27.
[27] C. F. Miller, G. W. Simmons, R. P. Wei, Scripta Materialia, 44 (2001) 2405-2410.
[28] L. Ma, K.-M. Chang, Scripta Materialia, 48 (2003) 1271-1276.
[29] C. F. Miller, G. W. Simmons, R. P. Wei, Scripta Materialia, 48 (2003) 103-108.
[30] C. J. McMahon Jr, Scripta Materialia, 54 (2006) 305-307.
[31] L. Viskari, Y. Cao, M. Norell, G. Sjöberg, K. Stiller, Materials Science and Engineering: A, 528 (2011) 2570-2580.
[32] L. Viskari, M. Hörnqvist, K. L. Moore, Y. Cao, K. Stiller, Acta Materialia, 61 (2013) 3630-3639.
[33] E. Maire, P. J. Withers, International Materials Reviews, 59 (2014) 1-43.
[34] B. Y. He, O. L. Katsamenis, B. G. Mellor, P. A. S. Reed, Materials Science and Engineering: A, 642 (2015) 91-103.
[35] H. Proudhon, A. Moffat, I. Sinclair, J.-Y. Buffiere, Comptes Rendus Physique, 13 (2012) 316-327.
[36] A. J. Moffat, B. G. Mellor, I. Sinclair, P. A. S. Reed, Materials Science and Technology, 23 (2007) 1396-1401.
[37] H. Toda, I. Sinclair, J. Y. Buffière, E. Maire, T. Connolley, M. Joyce, K. H. Khor, P. Gregson, Philosophical Magazine, 83 (2003) 2429-2448.
[38] H. Toda, I. Sinclair, J. Y. Buffière, E. Maire, K. H. Khor, P. Gregson, T. Kobayashi, Acta Materialia, 52 (2004) 1305-1317.

[39] D. J. Bull, A. E. Scott, S. M. Spearing, I. Sinclair, Composites Part A: Applied Science and Manufacturing, 58 (2014) 47-55.
[40] D. Proprentner, R. Jiang, P. A. S. Reed, L. G. Zhao, B. A Shollock, Study of oxidation mechamisms at fatigue crack tips using oxyen isotope tracer, under preparation (2016).
[41] Y. Tan, K. Kiekens, J. Kruth, A. Voet, W. Dewulf, Material dependent thresholding for dimensional X-ray computed tomography, International Symposium on Digital Industrial Radiology and Computed Tomography, (2011).
[42] T. L. Anderson, Fracture Mechanics: Fundamentals and Applications, Third Edition, CRC Press (2005).
[43] A. Karabela, L.G. Zhao, B. Lin, J. Tong, M.C. Hardy, Materials Science and Engineering: A, 567 (2013) 46-57.
[44] F. Farukh, L. Zhao, R. Jiang, P. Reed, D. Proprentner, B. Shollock, Mechanics of Advanced Materials and Modern Processes, 1 (2015) 1-13.